**NURETH14-068** 

#### TWO-PHASE FLOW AND CROSS-MIXING MEASUREMENTS IN A ROD BUNDLE

# A. Ylönen<sup>1</sup>, H.-M. Prasser<sup>1,2</sup>

<sup>1</sup> Paul Scherrer Institut, Nuclear Energy and Safety Research Department, Switzerland <sup>2</sup> Swiss Federal Institute of Technology, Zürich, Switzerland arto.yloenen@psi.ch, hprasser@ethz.ch

#### Abstract

The wire-mesh sensor technique has been used for the first time to study two-phase flow and liquid mixing in a rod bundle. A dedicated test facility (SUBFLOW) was constructed at Paul Scherrer Institut (PSI) in a co-operation with the Swiss Federal Institute of Technology (ETH Zürich). Simultaneous injection of salt water as tracer and air bubbles can be used to quantify the enhancement of liquid mixing in two-phase flow when the results are compared with the single-phase mixing experiment with the same test parameters. The second aspect in the current experiments is the two-phase flow in bundle geometry.

#### 1. Introduction

A research project was established at PSI in a co-operation with ETH Zürich. The main idea behind the current research was to study mixing and flow behavior inside a rod bundle using wire-mesh sensors (WMS). Adiabatic test facility with transparent test section was designed and built for this purpose. Series of single-phase tests was previously conducted [1]. The results proved that the WMS technique is suitable for the quantitative and qualitative characterization of liquid mixing inside the sub-channel and cross-mixing between the parallel sub-channels. In this paper, we will show its capability to be used for the liquid mixing studies in the presence of gas phase. Some non-intrusive methods are available for the void fraction measurements, but usually they lack the capability to measure flow distribution in high detail either in temporal or spatial sense.

Even though the WMS is a slightly intrusive measurement device, it offers an excellent way to measure void fractions and concentrations with high spatial and temporal resolution. The measurement technique applied in this study was developed in Rossendorf, Germany [2]. The basic working principle of the wire-mesh sensor is illustrated in Figure 1. The sensor consists of two wire layers, which together form the measurement grid. The lateral pitch of the wires, and the distance between the two wire layers, depends on how the sensor is used. To obtain a measurement, one transducer wire is excited at one time i.e. a voltage is applied. At the same time, currents are read from the receiver wires. The measured currents depend on the electrical conductivity of the fluid or fluid mixture between the transducer and receiver wires. Successively, all transducer wires are excited. After all transducer wires have been excited once, the read values are saved and a new measurement loop begins. Wire-mesh sensors are appropriate for both single-phase and two-phase experiments as long as there is a difference in

the electrical conductivities between the participating fluids. In the single-phase experiments, this conductivity difference is achieved by adding a so-called tracer liquid, which has distinctly different conductivity (higher/lower) compared to the main liquid.

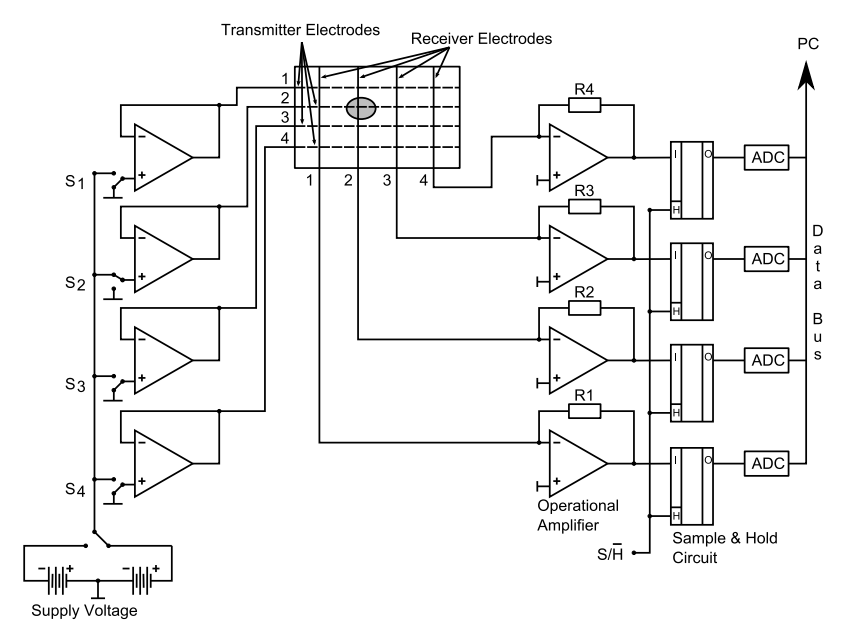


Figure 1 Working principle of the wire-mesh sensor

# 2. Experimental set-up

In this section, the different parts of test facility (SUBFLOW) are described in detail.

## 2.1 Test section and wire-mesh sensors

It was known from the earlier experience with wire-mesh sensors that a suitable lateral wire pitch of the electrode wires would be around 2 mm [3]. With a sensor size of 64×64 crossing points, a channel of 128×128 mm can be fully covered by a single sensor. Considering the fact that the critical bubble diameter for the inversion of the lift force, according to Tomiyama et al. [4], increases considerably if modeling the coolant in the reactor by an air-water flow, it was decided to increase the scale of the experimental set-up compared to a real fuel element accordingly. The scaling factor is approximately 2.6. Standard Plexiglas pipes (OD 25 mm, ID 19 mm), filled with de-mineralized water, were selected to simulate the fuel rods. For practical reasons, the central rod in the array was made of stainless steel. Salt water as tracer liquid can be isokinetically injected to the center of a sub-channel from the central rod. In order to minimize the disturbance of the flow in the sub-channel caused by injection capillary in each case, when a capillary below is used for injection, the capillaries (OD 1 mm, ID 0.5 mm) located at different heights are put into four different sub-channels, which are equal from the point of view of symmetry (B2, B3, C2 and C3); see Figure 2. In this way, 10 different elevations are realizable (Table 1). Injection location 8 was used in the experiments presented in this paper (emphasized in the table). Schematic drawing of the experimental set-up is also presented in Figure 2.

By upscaling, the pitch-to-diameter ratio of the rod bundle was kept similar to real fuel bundles as much as possible. In this regard, a pitch of 34 mm was chosen (P/D=1.36,  $D_h\approx30.3$  mm,  $D_\infty\approx33.9$  mm), and the parameters of the EPR (D=9.50 mm, P=12.6 mm) were chosen as reference values [5].

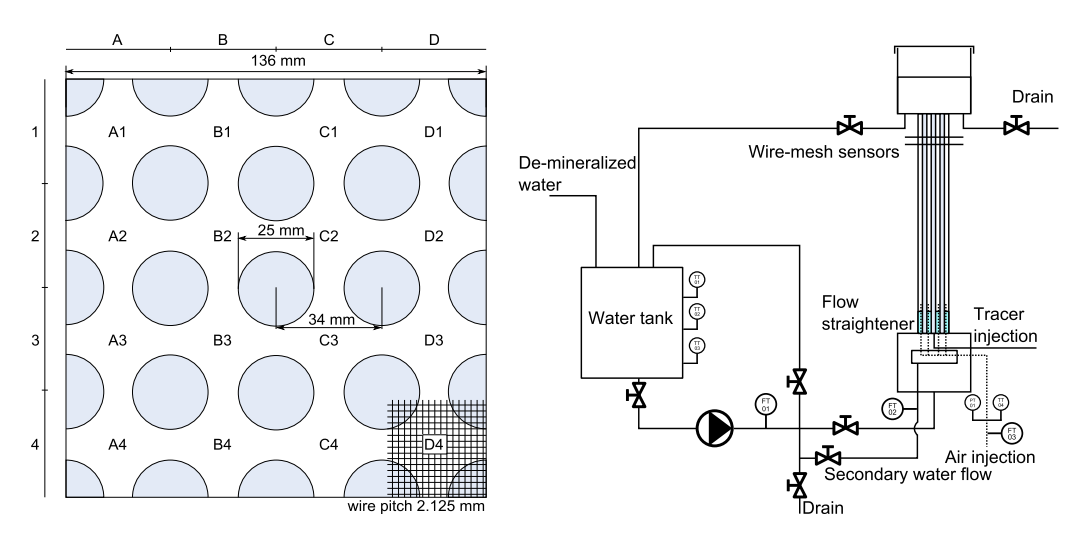


Figure 2 Top view of the test section and schematic drawing of SUBFLOW

No.	Distance from 1 <sup>st</sup> WMS [mm]	Sub-channel
NO.	Distance from 1 www.s [mm]	Sub-channel
1	35	B2
2	70	C2
3	140	C3
4	245	В3
5	385	B2
6	560	C2
7	770	C3
8	1015	В3
9	1295	B2
10	1610	C2

Table 1 Locations of the tracer liquid injection points

The chosen bundle parameters resulted in a square channel with an inner cross-section of  $136 \times 136$  mm. Using 64 transmitting and 64 receiving wires, covering the whole channel cross section, in total 2304 active measuring points were created between the rods, meaning 144 points for each sub-channel. By splitting the transmitter outputs of the sensor electronics unit, it is possible to operate a pair of such sensors as one sensor of the dimensions  $64 \times 128$ , with 2.5 kHz measurement frequency. The signals for each sensor are separated later during data processing. In the current wire-mesh sensors, the exact lateral pitch of the wires is 2.125 mm. For the electrodes, stainless steel wires of 0.1 mm diameter were used. The distance between the wire layers in the sensor was set as 2 mm. The axial distance between the two wire-mesh sensors was 15 mm in this study. More detailed description of the test section and designed wire-mesh sensors can be found from the previous publication by the authors [1]. The overall view of the test facility and drawing of the test section are presented in Figure 3.

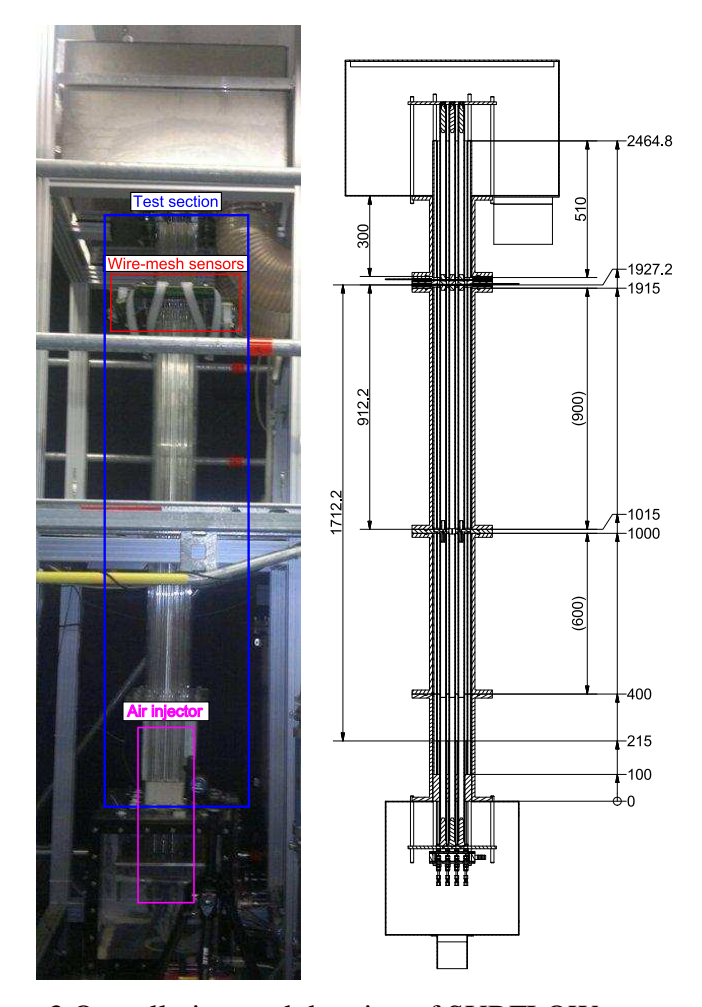


Figure 3 Overall view and drawing of SUBFLOW test section

#### 2.2 Air injection system

Special air injection system was developed in order to inject the same amount of air and similar bubbles in all of the 16 sub-channels. The conceptual design was adopted from the test facility, which was also previously located at PSI [6]. The injection system has a water collector, 16 water tubes (OD 6 mm, ID 4 mm), and for each of the water tubes also an air capillary (OD 0.8 mm, ID 0.6 mm). Air injector is located in the test section app. 171 cm upstream from the first wire-mesh sensor. Bubble size can be varied by changing the secondary water flow rate i.e. the water flow through the water tubes. The secondary water flow rate was adjusted by the manual ball valve and was between 930-990 l/h in all the tests. Small bubbles can be generated by increasing the secondary water flow and large bubbles by decreasing or even stopping it. The drawing of the air injector is presented in Figure 4. Sample images from the injector outlet for test series 3 are shown in Figure 5. The air and secondary water flow rates are the parameters that have the most significant effect to the bubble diameter. The main flow rate seems to have only an effect to bubble shapes i.e. higher flow rate tends to elongate large bubbles. Bubble diameters vary from 3-4 mm in the first case, 5-6 mm in the second case and more than 10 mm in the third case.

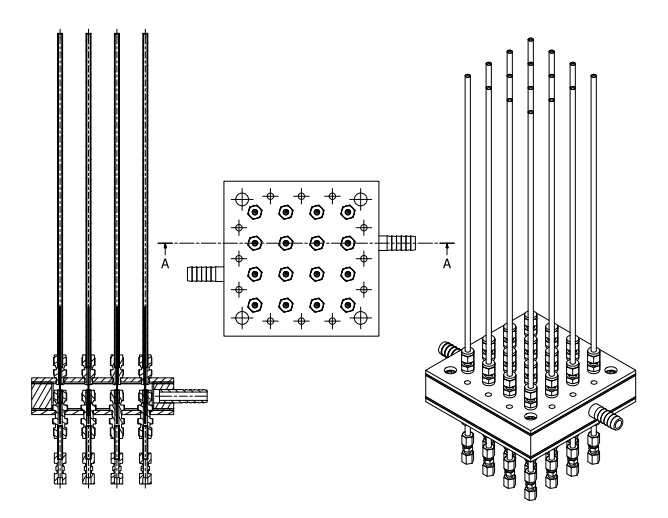


Figure 4 Air injector

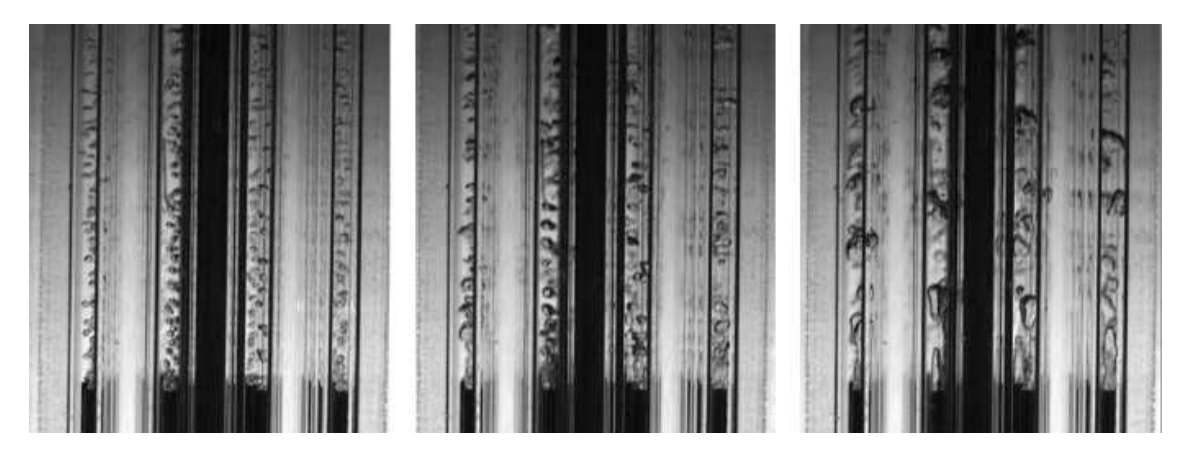


Figure 5 Images from the air injector outlet, TS 3,  $J_G$ =0.008 m/s (left),  $J_G$ =0.020 m/s (center),  $J_G$ =0.039 m/s (right)

# 3. Experimental results

In this section, the results from the series of two-phase mixing experiments are described in detail. Test matrix for the performed experiments can be found in Table 2. The main flow rate of water was the parameter that was varied between the test series (TS). Same air flow rates were covered in all the series.

#### 3.1 Conversion of measurement values

Raw measurement data can be converted to various values and analyzed in several ways. The wire-mesh electronic units use a 12-bit analog-to-digital converter (ADC), which results in a measurement range of integer values from 0 to 4079. We will describe next the conversion and analysis methods that are applied to obtain the results presented in this paper. The duration of each measurement was 30 seconds with 2.5 kHz measurement frequency. However, the analyses were performed for 20 seconds of the experiment to reduce the size of the data arrays that need to be handled.

No.	$Q_L [m^3/h]$	<b>J</b> <sub>L</sub> [m/s]	Q <sub>G</sub> [ln/min]	$J_G$ [m/s]	Volumetric quality (inlet) β
1	21.95	0.57	0	0	0
			5	0.008	0.0135
			12.5	0.020	0.0330
			25	0.039	0.0640
2	42.97	1.12	0	0	0
			5	0.008	0.0069
			12.5	0.020	0.0172
			25	0.039	0.0337
3	58.29	1.52	0	0	0
			5	0.008	0.0051
			12.5	0.020	0.0127
			25	0.039	0.0251

Table 2 Test matrix for two-phase mixing experiments

## 3.1.1 Dimensionless mixing scalar

To transform measurement values to dimensionless mixing scalars representing the degree of mixing, a calibration with a plain tracer liquid of known electrical conductivity has to be carried out. However, in this case calibration was done using a reference liquid i.e. water that has significantly higher electrical conductivity than de-mineralized water, but not high enough to saturate the measurement signal. A fresh calibration point for the main flow (demineralized water, DMW) can be easily obtained by recording the signals of the sensor for a couple of seconds before each tracer injection. Calibration values for reference liquid (R) can be measured, for example, once in the test series. Using these values, the dimensionless mixing scalar can be determined from the measured value from

$$\Theta_{i,j,k} = \frac{I_{i,j,k} - I_{DMW,i,j}}{I_{R,i,j} \left(\sigma_{tracer} / \sigma_{reference}\right) - I_{DMW,i,j}}$$
(1)

where  $\Theta_{i,j,k}$  is the local instantaneous dimensionless mixing scalar,  $I_{i,j,k}$  is the current value measured for the mixture at the crossing point i,j at the instant k.  $I_{DMW,i,j}$  and  $I_{R,i,j}$  are time-averaged measurement values for calibration cases for the crossing point i,j. Additionally, the ratio of tracer ( $\sigma_{tracer}$ ) and reference ( $\sigma_{reference}$ ) electrical conductivities was introduced into the dimensionless mixing scalar equation to normalize the measurement values. If the signal value is higher than the calibration value for de-mineralized water, tracer liquid is assumed to be present and dimensionless mixing scalar is calculated, otherwise  $\Theta_{i,j,k}$ =0.

Local time-averaged dimensionless mixing scalars are calculated by knowing the sum of time-instances when liquid was present for each crossing-point of the sensor.

$$\overline{\Theta}_{i,j} = \frac{1}{n_{liauid}} \sum_{k=1}^{n} \Theta_{i,j,k}$$
 (2)

where n is the number of measurement frames and  $n_{\text{liquid}}$  is the sum of time instances when liquid was present at that crossing-point. The results from the two-phase mixing experiments are compared with the single-phase mixing experiments.

#### 3.1.2 Void fraction

In two-phase experiments measurement values for liquid phase have to be separated for those of gas phase. During the experiments, the values for the amplification are adjusted in a way that a noticeable baseline level is measured in the presence of de-mineralized water. If the signal value is less than this baseline, some air is connecting the wire layers. Instantaneous void fractions are calculated from

$$\alpha_{i,j,k} = \frac{I_{i,j,k} - I_{DMW,i,j}}{I_{Air,i,j} - I_{DMW,i,j}} \cdot 100\%$$
(3)

We can assume air as perfect insulator  $(I_{Air,i,j}\approx 0)$ . If the signal value is above the baseline, naturally instantaneous void fraction is then  $\alpha_{i,j,k}=0$ . In order to filter out some electrical noise, low void fraction values (<10%) are excluded and set as zero. However, the presence of tracer liquid brings some difficulties to extract void fraction distribution since the zero void signal value increases significantly. Therefore, two-phase experiments without tracer injection were also conducted and the void fraction profiles were extracted from those tests. The reproducibility of the two-phase experiments is considered to be good on the basis of comparison of void fraction profiles from the other sub-channels (not injection sub-channel). Local time-averaged void fraction can be calculated from the converted void fraction values with

$$\overline{\alpha}_{i,j} = \frac{1}{n} \sum_{k=1}^{n} \alpha_{i,j,k} \tag{4}$$

where n is the number of measurement frames and  $\alpha_{i,j,k}$  is the instantaneous void fraction for the crossing point i,j at the instant k. The results from the two-phase experiments are presented in the sections 3.2-3.5. The receiver wire number 63 of the first wire-mesh sensor is excluded from the analysis as a broken wire (white line in the plots). As it is next to the channel wall, the effect to the results is practically negligible.

# 3.1.3 Velocity and volume of individual bubble

In order to obtain the velocities for all the bubbles, some numerical procedures are needed. The first step is to convert all measurement values to void fraction values and split the results to two arrays (two sensors). The second step is to detect all the bubbles on the first wire-mesh sensor. The extended decremental fill method is used for the identification of the bubbles [7]. All bubbles are assigned with unique bubble number and they are saved in the array as large as the void fraction array. The third step is to cross-correlate the void fraction data between the two wire-mesh sensors. The cross-correlation is done with the "fine correlation" method described by Simiano and Prasser [8]. In all simplicity it means that for each of the identified

bubbles average void fraction and standard deviation of the void fraction are calculated. It is assumed that the shape of bubble remains unchanged between the sensors so we can calculate same values from the void fraction data of the second sensor for that volume. Normalized cross-correlation coefficient can be calculated between the two wire-mesh sensors. We introduce a time shift for the cross-correlation to obtain the time-of-flight in frames. The maximum correlation coefficient and delay in frames are saved in the output file. The velocity can be approximated from the delay since we know the distance between the two sensors (15 mm). Since we know approximately what should be the range of velocities, we can manually set some limits for the time delay to avoid unrealistically low and high bubble velocities caused by the errors in the cross-correlation procedure.

Now as we have obtained the velocities of the bubbles, we can calculate equivalent diameters [9]. The approximated volume of the bubble can be calculated from the equation

$$\widetilde{V}_{\text{Bub}} \cong w_{\text{Bub}} \Delta x \Delta y \Delta t \sum \alpha_{i,j,k} \forall (i,j,k) \in \text{Bubble}$$
 (5)

where  $w_{Bub}$  is the velocity of the bubble,  $\Delta x$  and  $\Delta y$  are the spatial resolutions in x- and y-directions (2.125 mm) and  $\Delta t$  is the time interval between two successive frames (0.0004 s). Last term is the sum of void fractions that belong to the analyzed bubble. Equivalent diameter can be obtained from the equation

$$D_{\rm Bub} = \sqrt[3]{\frac{6\widetilde{V}_{\rm Bub}}{\pi}} \tag{6}$$

Bubble diameter can be used to generate void fraction distribution plots for different equivalent bubble diameters (section 3.3).

## 3.2 Void fraction distribution inside the rod bundle

Two-phase experiment was performed for each flow condition in the test matrix (Table 2). Time-averaged void fraction distributions are presented in Figure 6. Each of the square dots present one crossing-point of the wire-mesh sensor. As pictured already in Figure 5, used three air flow rates result in three distinctly different initial bubble diameters. In the first case bubbles are small enough to be attracted by the rods. Clear wall peaks are observed in all test series. However, bubbles are pushed more to the rod walls as the main flow rate (Q<sub>L</sub>) is increased. In the second case, larger bubble diameter changes void fraction distribution significantly and we obtain central peaks instead of wall peaks. The reversal of the lift force is causing this behavior. In the third case, initial bubbles are even larger and elongated. Distributions change slightly from the second case as higher void fractions are also measured from the rod gaps. In addition, secondary flows in non-circular flow channel might have some influence to void fraction distribution. Figure 7 shows that the time-averaged void fraction distributions are almost identical between the two wire-mesh sensors despite the fact that the wires of the first sensor slice the bubbles in many smaller bubbles. Naturally due to this fact, the maximum time-averaged void fraction values are a bit lower than from the first sensor.

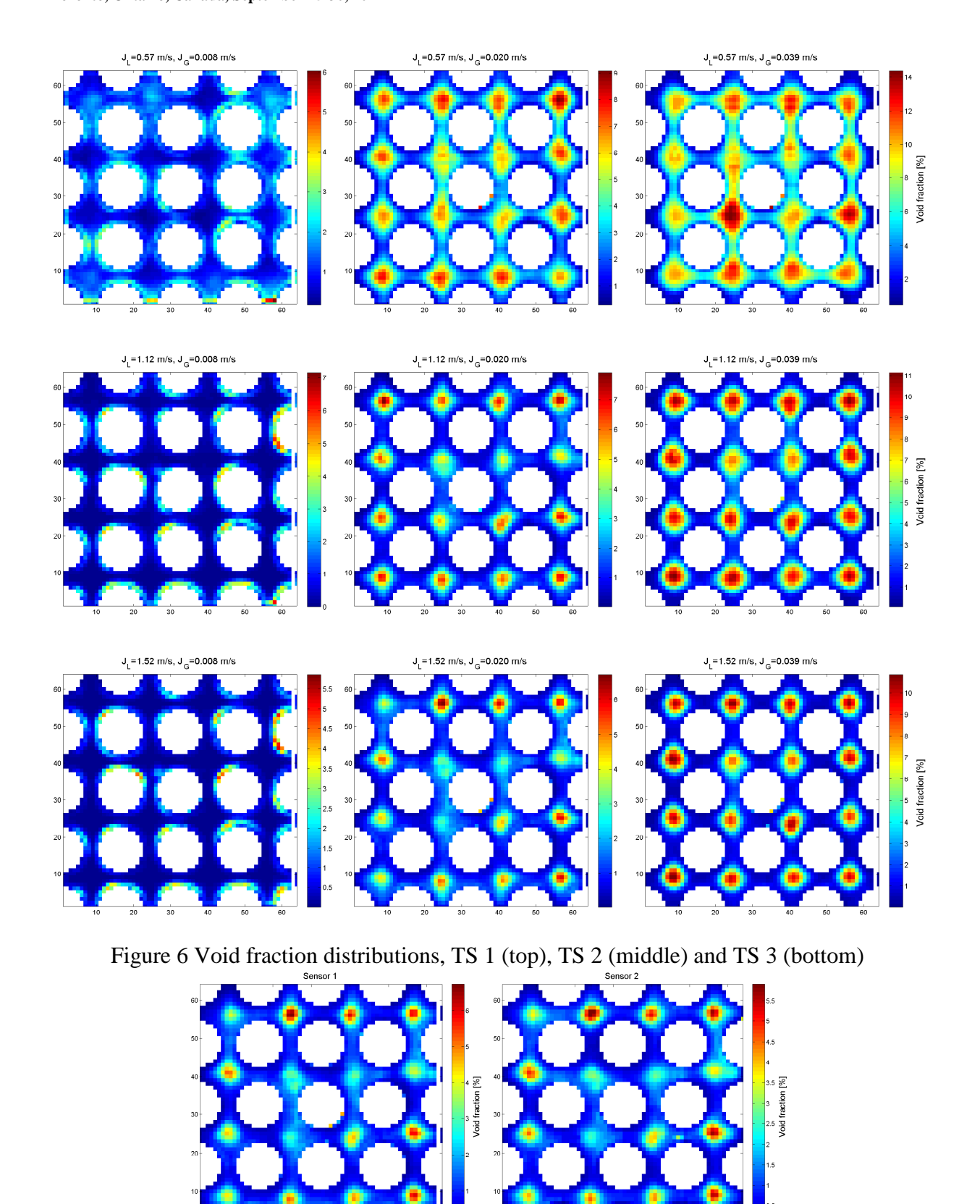


Figure 7 Void fraction distribution comparison between the sensors, TS 3,  $J_G$ =0.020 m/s

# 3.3 Void fraction distribution inside the rod bundle by the bubble diameter

After the bubble identification and cross-correlation processes, all the bubbles have unique bubble numbers and velocities are known. Approximated volume of the bubble and equivalent diameters are obtained as it was described in the section 3.1.3. We can now define diameter ranges and calculate the void fraction distribution for those ranges. The bubbles that don't belong to this diameter range are excluded from the void fraction array. The second experiment ( $J_G$ =0.020 m/s) in test series 3 is analyzed in more detail and the void fraction distributions for four diameter ranges are presented in Figure 8. The defined ranges show the effect of lift force to the void fraction distribution. The plots also show that the tracer injection capillaries might have some effect to the bubble diameters in the four inner sub-channels. In the future, tests without capillaries will be conducted.

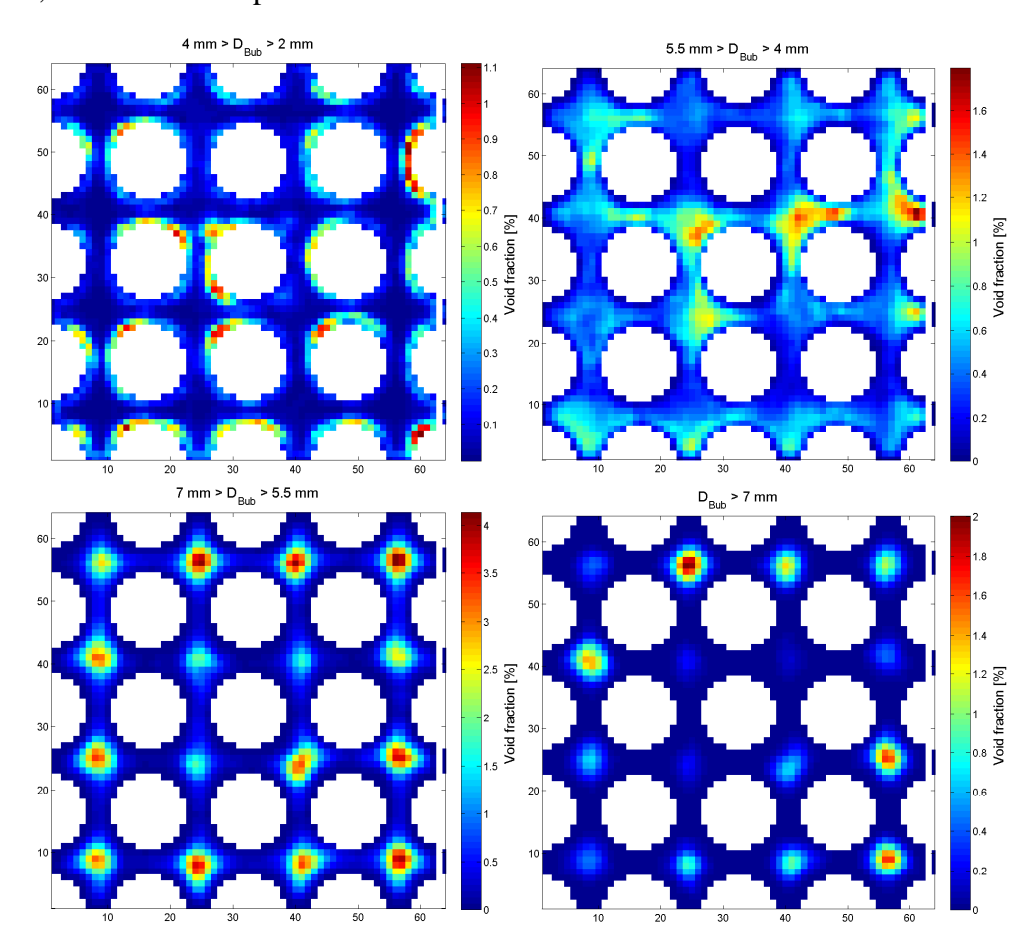


Figure 8 Void fraction distributions for different bubble diameter ranges, TS 3, J<sub>G</sub>=0.020 m/s

## 3.4 Average gas velocities inside the rod bundle

There are two ways to estimate average gas velocities. Traditional way is to do cross-correlation between two sensors for each cross-point and to use the delay to calculate average gas velocity. More complex method is to calculate the average from the velocities of individual bubbles. The results obtained in this way are presented in Figure 9. Since very few

bubbles are travelling in the middle of the sub-channels in the first test ( $J_G$ =0.008 m/s), the averaged values are not changing that smoothly compared to the other tests. The average gas velocities are much lower near the rods in all the tests. The "cut-off velocities" 1.07 m/s and 2.21 m/s were manually introduced to cross-correlation procedure to avoid unrealistically low and high bubble velocities.

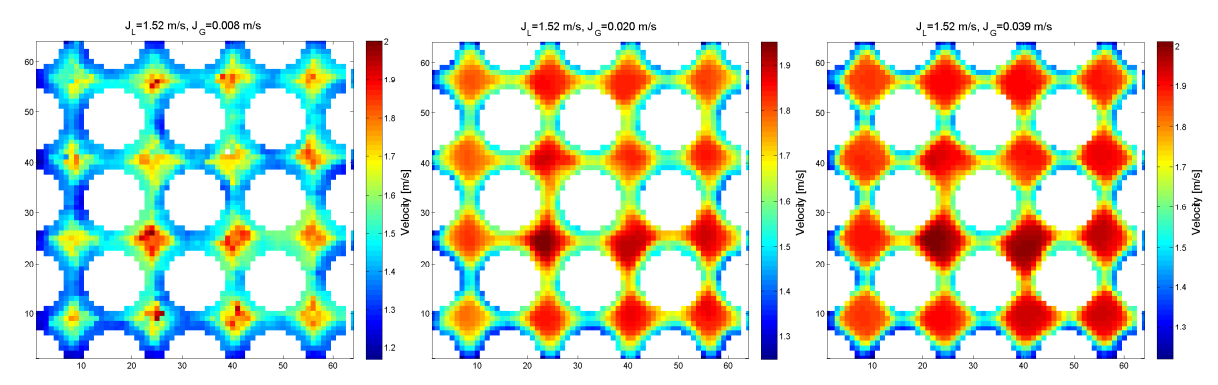


Figure 9 Average gas velocities, TS 3

# 3.5 Bubble size distributions

Test series 3 was analyzed in detail and the obtained bubble size distributions are presented in Figure 10. Size probability density functions (left) show the distribution of bubbles between different bubble diameters. In the first test we get single peak distribution with the average diameter of 3.25 mm. In the second test we see two peaks, one below the critical bubble diameter and one above. Average diameter of the bubbles is 4.36 mm. In the third test we see large number of small bubbles, but also some small peaks in large diameters (>10 mm). However, due to the large quantity of small bubbles, average bubble diameter remains quite small, 4.54 mm. Volume probability density functions (right) show how volume of bubbles in different bubble classes contribute to the combined volume of all bubbles. Single peaks are obtained for the first two tests. In the third test we see now clearly that the small number of large diameter bubbles have significant contribution to the total volume of the bubbles. Cutoff diameter of 2 mm was used since the bubbles smaller than that can't be detected reliably by the sensors due to limited spatial resolution of the sensor grid (i.e. sub-resolution bubbles).

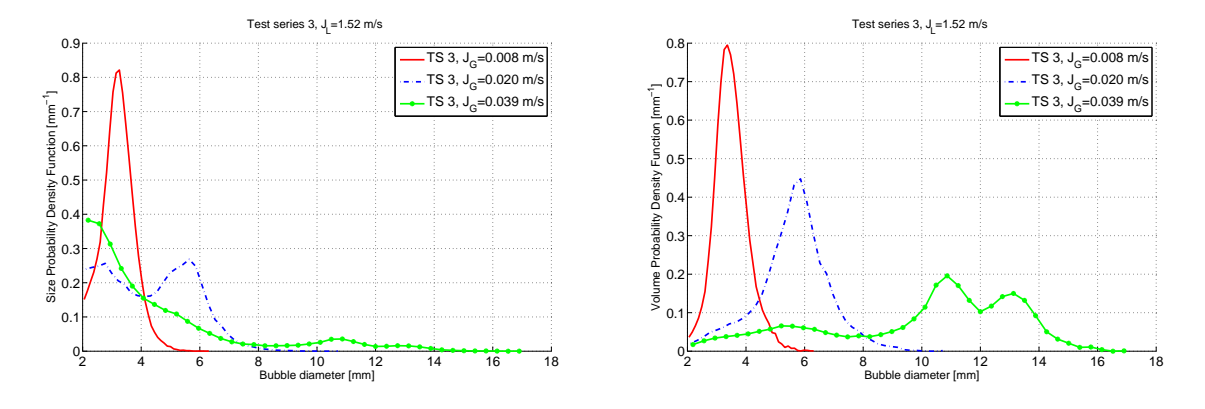


Figure 10 Size (left) and volume probability density functions (right), TS 3

## 3.6 Distribution of tracer liquid inside the rod bundle

Dimensionless mixing scalars are converted from the raw measurement data as described in the section 3.1.1. The injection location 8 was selected for the experiments since mixing inside the injection sub-channel should be almost complete in that point. However, the characteristic behavior of the wire-mesh electronics unit makes it difficult to directly compare time-averaged dimensionless mixing scalars from the single- and two-phase experiments. Therefore, time-averaged values are renormalized by the sum of time-averaged dimensionless mixing scalars from that experiment. The low threshold of 0.000015 was applied for the dimensionless mixing scalars before the summation to reduce the effect caused by the noise. In this way we obtain tracer distribution profiles for the experiments and they can be qualitatively compared with each other. Renormalized time-averaged dimensionless mixing scalar profiles from the one measurement line (number 25) of the first WMS are presented in Figure 11. The measurement line goes through the injection sub-channel. The graphs show how the increase of air flow rate flattens the profiles. This effect is the most visible with the lowest liquid flow rate. The behavior shows to which extend the bubbles promote the liquid mixing inside the injection sub-channel and between the parallel sub-channels.

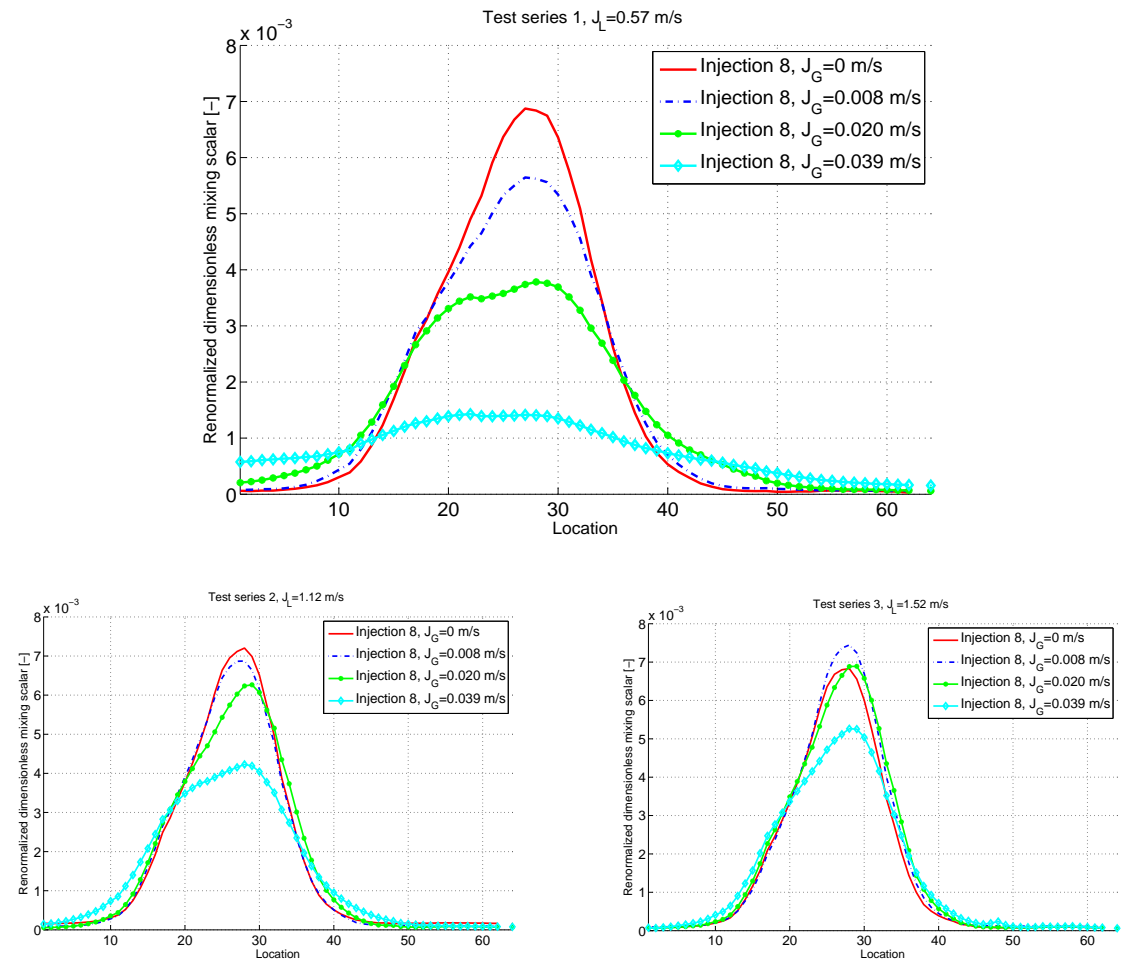


Figure 11 Renormalized time-averaged dimensionless mixing scalar profiles, TS 1 (top), TS 2 (bottom left), and TS 3 (bottom right)

# 4. Conclusions

Two-phase measurements in the SUBFLOW test facility provide unique void fraction data for the code validation purposes. Especially the obtained bubble size distributions are valuable information for the validation of so-called MUltiple SIze Group (MUSIG) models. This information together with the void fraction and average gas velocity profiles gives an insight view of two-phase flow inside a rod bundle. The possibility to study void fraction distributions for different bubble diameter ranges shows the transition from the wall peak to the central peak due to the reversal of the lift force. Two-phase mixing experiments show qualitatively that the bubbles promote significantly the mixing of the liquid inside the injection sub-channel and between the parallel sub-channels.

# 5. References

- [1] Ylönen, A., Bissels, W.-M. and Prasser, H.-M. "Single-phase cross-mixing measurements in a 4x4 rod bundle," *Nuclear Engineering and Design* (241), 2011, pp. 2484-2493.
- [2] Prasser, H. -M., Böttger, A. and Zschau, J. "A new electrode-mesh tomograph for gasliquid flows," *Flow Measurement and Instrumentation* (9:2), 1998, pp. 111 119.
- [3] Lucas, D., Krepper, E. and Prasser, H.-M. "Development of co-current air-water flow in a vertical pipe," *International Journal of Multiphase Flow* (31:12), 2005, pp. 1304 1328.
- [4] Tomiyama, A., Tamai, H., Zun, I. and Hosokawa, S. "Transverse migration of single bubbles in simple shear flows," *Chemical Engineering Science* (57:11), 2002, pp. 1849 1858.
- [5] EPR Brochure, Areva, May 2005.
- [6] Milenković, R. Ž. "Experimental Investigation of Bubbly Jets," PhD thesis, ETH Zurich, 2005.
- [7] Prasser, H. -M., Beyer, M. "Bubble recognition algorithms for the processing of wiremesh sensor data," <u>Proceedings of 6<sup>th</sup> International Conference on Multiphase Flow ICMF 2007</u>, Paper No. 719, Leipzig, Germany, 2007 July 9-13.
- [8] Simiano, M. and Prasser, H. -M. "Estimation of individual bubble velocities in a gasliquid flow using wire-mesh sensors," <u>Proceedings of 6<sup>th</sup> International Conference on Multiphase Flow ICMF 2007</u>, Paper No. 458, Leipzig, Germany, 2007 July 9-13.
- [9] Prasser, H. -M., Scholz, D. and Zippe, C. "Bubble size measurement using wire-mesh sensors," *Flow Measurement and Instrumentation* (12), 2001, pp. 299 312.